Electronic Supplementary Material (ESI) for Journal of Materials Chemistry A.

Supplementary Information

Biomimicry of *Cuscuta* Electrode Design Endows Hybrid Capacitor with Ultrahigh Energy Density Exceeding 2 mWh cm^{-2} at a Power Delivery of 25 mW cm^{-2}

Ying-Chu Chen, [a] *Yan-Gu Lin* [b] *and Yu-Kuei Hsu* [c]*

Ying-Chu Chen
[a]Karlsruhe Institute of Technology (KIT), Institut für Anorganische Chemie, Engesserstraße 15, D-76131 Karlsruhe, Germany
Yan-Gu Lin
[b]National Synchrotron Radiation Research Center, Hsinchu 30076, Taiwan
E-mail: lin.yg@nsrrc.org.tw
Yu-Kuei Hsu
[c]Department of Opto-Electronic Engineering, National Dong Hwa University, Hualien 97401, Taiwan
E-mail: ykhsu@mail.ndhu.edu.tw

Experimental section

Materials. Carbon cloth (B-1, Designation A: plain-weave, 116 g m^{-2}, thickness 0.35 mm; no wet-proofing) functioning as host material in a hybrid supercapacitor electrode from E-TEK Division, USA. Ammonium metavanadate (NH_4VO_3, ≥ 99 %, Sigma-Aldrich), anhydrous sodium sulfate (Na_2SO_4, 99 %, Sigma-Aldrich) served as precursors for monohydrated vanadium pentoxide ($V_2O_5 \cdot H_2O$) preparation. All precursor solutions were prepared with deionized water of resistivity not less than 18.2 MΩ cm. To evaluate electrochemical properties we employed 1-ethyl-3-methylimidazolium chloride ([EMIM][Cl], 98 %, Sigma-Aldrich) and bis(trifluoromethane) sulfonimide lithium salt (LiTFSI, 98 %, Alfa Aesar) as starting materials to prepare a room-temperature ionic liquid, 1-ethyl-3-methylimidazolium bis(trifluoromethanesulfonyl)imide ([EMIM][TFSI]) as electrolyte. Dichloromethane (CH_2Cl_2, ≥ 98 %, Sigma-Aldrich) and deionized water served as solvent for the preparation of [EMIM][TFSI]. All chemicals used in this work were of analytical grade and used without further purification.

Preparation of $V_2O_5 \cdot H_2O$/CC Electrode. Carbon cloth (CC) serving as host framework was first cut into pieces with working area 3 cm x 0.5 cm and then attached to a copper wire at the short edge. The junction was next covered with silver paste to ensure a well conducting circuit for subsequent electroplating. The connecting pad was coated with epoxide to prevent undesirable side reactions. After the pretreatments, carbon cloth was subjected to electrodeposition on immersion into the precursor solution with a nominal area controlled to be 1 cm^2. The precursor solution consisted of ammonium metavanadate (0.26 M), to which sodium sulfate was added as supporting electrolyte. A three-electrode configuration with prepared carbon cloth as working electrode, Pt foil as counter electrode and Ag/AgCl electrode in potassium chloride (KCl, 3 M) solution as reference electrode was employed for electrodeposition. The electroplating was implemented under diverse constant current flows for 12 h at 70 °C. For the synthesis reported here, the electroplating current density was varied from 1 to 2 mA cm^{-2}; the concentration of sodium sulfate was varied from 0 to 2 M. The specimens as grown were rinsed with distilled water several times to remove residual precursors and subjected to drying under vacuum to remove moisture. A potentiostat (CHI 627D, CH Instruments) was used for electrodeposition and all subsequent electrochemical tests. The mass uptake of $V_2O_5 \cdot H_2O$ was determined using a microbalance (Sartorius BP 211D, Germany, accuracy 10 μg).

Synthesis of Ionic Liquid. Experimental conditions for the [EMIM][TFSI] synthesis followed the methods described in the literature, with modifications.[1] To an aqueous solution of 1-ethyl-3-methylimidazolium chloride (74.8 g, 0.5 mol), lithium bis(trifluoromethane sulfonyl)imide was added (161.2 g, 0.55 mol) and stirred at 23 °C for 30 min to afford a biphasic solution. The organic phase was then separated, diluted with dichloromethane and washed with distilled water several times until the remaining chloride ions were undetectable with a $AgNO_3$ solution. Dichloromethane was first removed from the solution *via* distillation under vacuum at 80 °C overnight. Subsequently, the solution was dried under vacuum at 150 °C for several hours to remove residual water (yield: 80 %). The purified [EMIM][TFSI] ionic liquid was stored under an Ar atmosphere before use.

Characterization of $V_2O_5{\cdot}H_2O$/CC Electrode. The nanostructural and microtextural evolutions of $V_2O_5{\cdot}H_2O$/CC electrodes under varied conditions of preparation were examined with a field-emission scanning electron microscope (FESEM, Zeiss Supra 40 VP). To evaluate the growth kinetics, a small amount of $V_2O_5{\cdot}H_2O$/CC electrodes at varied stages of synthesis and interval 6 h was also collected and characterized with the FESEM. The dimensions and geometry of $V_2O_5{\cdot}H_2O$ were confirmed with a transmission electron microscope (Philips/FEI CM200, accelerating voltage 200 kV). X-ray powder diffraction (XRD, Stoe STADI-P diffractometer) with Ge-monochromatized Cu-$K_{\alpha 1}$ radiation (40 kV, 40 mA) was applied to identify the crystal phase of specimens. The electrochemical properties of $V_2O_5{\cdot}H_2O$/CC electrodes were evaluated with cyclic voltammetric (CV) and galvanostatic charge or discharge (GCD) methods and AC impendence analysis. All measurements were performed with a three-electrode system containing $V_2O_5{\cdot}H_2O$/CC electrodes as working electrode, Pt foil as counter electrode and Ag/AgCl reference electrode. The evaluations were conducted in neat [EMIM][TFSI] ionic liquid.

Fabrication of Symmetric Supercapacitor. A symmetric supercapacitor was built in a two-electrode configuration: an [EMIM][TFSI]-soaked PTFE membrane separator (WL Gore & Associates) was sandwiched between two identical $V_2O_5{\cdot}H_2O$/CC electrodes. Each electrode had the same working area; the dimensions of the fabricated module were length 2 cm, width 0.5 cm, height 0.1 cm. Cyclic voltammetric and galvanostatic charge or discharge analyses were adopted to estimate the electrochemical performance. All operating current densities were normalized to the nominal area, namely 1 cm^2, of the symmetric device.

Calculation. Footprint-normalized capacitance of $V_2O_5{\cdot}H_2O$/CC electrode in [EMIM][TFSI] ionic liquid was calculated from their cyclic voltammetries according to this equation,

$$C_s = \frac{\int I dV}{v \Delta V A} \tag{1}$$

in which C_s (F cm^{-2}) is the specific capacitance normalized to effective area, I (A) is the current of the discharge curve integrated with respect to the potential V, v (V/s) is the charge-discharge rate of the scan, ΔV (V) is the potential window for the scan, and A (cm^2) is the nominal area of electrode.

Alternatively, the footprint-normalized capacitance was derived from the galvanostatic charge or discharge curve based on the following formula,

$$C_s = \frac{I}{(\Delta V/\Delta t)A} \tag{2}$$

in which I (A) is the applied current, ΔV (V) is the potential sweep range, Δt (s) is the discharge time after initial iR drop and A (cm^2) is the nominal area of an electrode.

Likewise, the footprint-normalized capacitance of symmetric $V_2O_5 \cdot H_2O$ supercapacitor was estimated from the galvanostatic charge or discharge curve with this equation,

$$C_{SSC} = \frac{I}{(\Delta V_{Cell}/\Delta t)A_{Cell}} \tag{3}$$

in which C_{SSC} (F cm^{-2}) is the specific capacitance, I (A) is the applied current, ΔV_{Cell} (V) is the cell voltage, Δt (s) is the discharge time after initial iR drop and A_{Cell} (cm^2) is the nominal area of a module.

The footprint-normalized energy and power delivery of symmetric $V_2O_5 \cdot H_2O$ supercapacitors were derived from these equations,

$$E = \frac{1}{2} C_{SSC} \Delta V_{Cell}^{2} \times \frac{1000}{3600} \tag{4}$$

$$P = \frac{\Delta V_{Cell}^{2}}{4 R_{ES} A_{Cell}} \times 1000 \tag{5}$$

in which E (mWh cm^{-2}) is the energy density normalized to nominal area of module, C_{SSC} (F cm^{-2}) is the specific capacitance of a module, ΔV_{cell} (V) is the cell voltage, P (mW cm^{-2}) is the power density normalized to nominal area of a module, A_{cell} (cm^2) is the nominal area of a module and R_{ES} (Ω) is the equivalent series resistance calculated according to this formula,

$$R_{ES} = \frac{\Delta V_{iR}}{2I} \tag{6}$$

in which ΔV_{iR} (V) is the voltage drop occurring in the galvanostatic charge or discharge curve as current polarity switched and I (A) is the applied current.

Dependency of ion-mobility-relevant EDLC on the physical properties of carbon hosts. The working principle of electrical double layer capacitance (EDLC), in which the electrode stored charge via a physical ion adsorption/desorption process at the polarized-electrode/electrolyte interface, can well describe the ion diffusion behavior within the substrate framework. Herein, we summarized carbon nanofoam (CNF) and laser-induced graphene (LIG), in addition to carbon cloth (CC) employed in this study, for discussion because they were well acknowledged as highly promising substrates for supercapacitor application.[2-5] In particular, LIG was prevalently employed as the substrate in a micro-capacitor fabrication, bearing a thickness of few tens of mircrometre that is the thinnest host among these representatives (Table 1 in the main text).

However, LIG demonstrated the lowest area-normalized EDLC of ~ 10 mF cm^{-2} (Fig. S1a). By contrast, CC had a thickness up to 330 μm greatly exceeding that of LIG nearly one order of magnitude whereas its areal capacitance (52 mF cm^{-2}) only quintupled that of LIG. Surprisingly, CNF bore a moderate thickness yet exhibited the highest areal capacitance up to 560 mF cm^{-2}, which was higher than those of CC and LIG by a factor more than 10. Evidently, the areal capacitance of the substrate was not dictated by its geometric thickness. Such contrast originated highly likely from the pore-size distribution, in which LIG had a characteristic mesopore-size below 9 nm greatly limiting ion diffusion in those porous tunnels (Table 1 in the main text). The interplay between surface area and pore-size distribution substantially determines the quantity of interface available for ions and concomitant geometric EDLC of the substrate (Fig. S1b). Those accessible surface area in turn served as nucleation sites to load pseudocapacitive materials in a conventional hybrid electrode preparation protocol (Table S1).

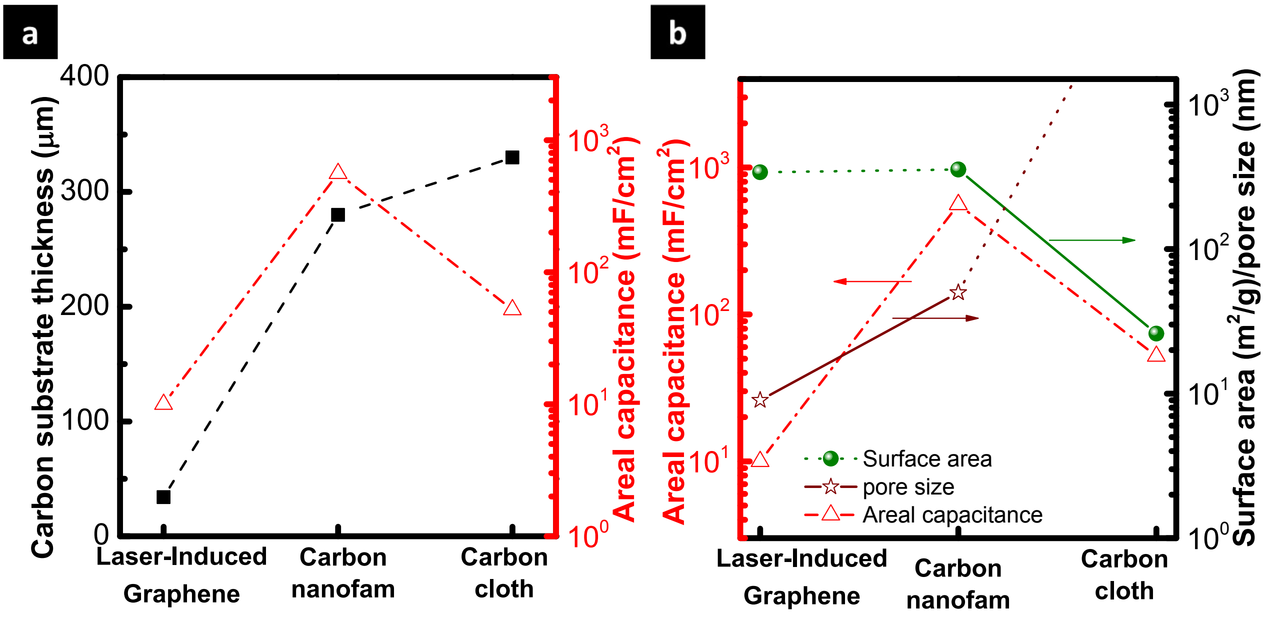

Fig. S1 (a) Areal capacitances collected in aqueous electrolyte of diverse carbonaceous substrates. The geometric thickness was plotted alongside for reference (black line). (b) Dependency of areal electrode capacitance on mean pore-size and surface area of various carbon frames. Solid lines in those properties indicated the major dominator in determining the areal capacitance.

Table S1. Dependency of areal and volumetric capacitances on the mass uptake of electroactive oxides.

Electrode	**Oxide Weight %**[a]	**Areal capacitance**	**Volumetric capacitance**	**Ref.**
FeOOH/CNF	16%	280 mF/cm^2	40 F/cm^3	4
FeOOH$_x$/CNF	27%	850 mF/cm^2	121 F/cm^3	
MnO$_2$/CNF	~ 45 %	1400 mF/cm^2	81 F/cm^3	5
MnO$_2$/CNF	~ 40 %	1500 mF/cm^2	90 F/cm^3	
V$_2$O$_5$·H$_2$O/CC	72%	2657 mF/cm^2	81 F/cm^3	This work

[a] Oxide weight percent was derived from the areal mass density of active oxides normalized to that of overall electrode inklusive of underlying carbon hosts.

It is worth to mention that the geometric capacitance, including areal and volumetric capacitances, concurrently enhanced upon increasing the mass intake of pseudocapacitive substance, as evidenced in the reports by Long et al. in manganese- and iron-based oxide systems.[4-5] One should keep in mind that such phenomenon is indeed opposite to the effect of device engineering, in which the volumetric capacitance enhanced at the sacrifice of areal performance.[6] Significantly, the bioinspired protocol in this study realized the highest oxide loading and most importantly, the best areal capacitance at a satisfactory volumetric capacitance.

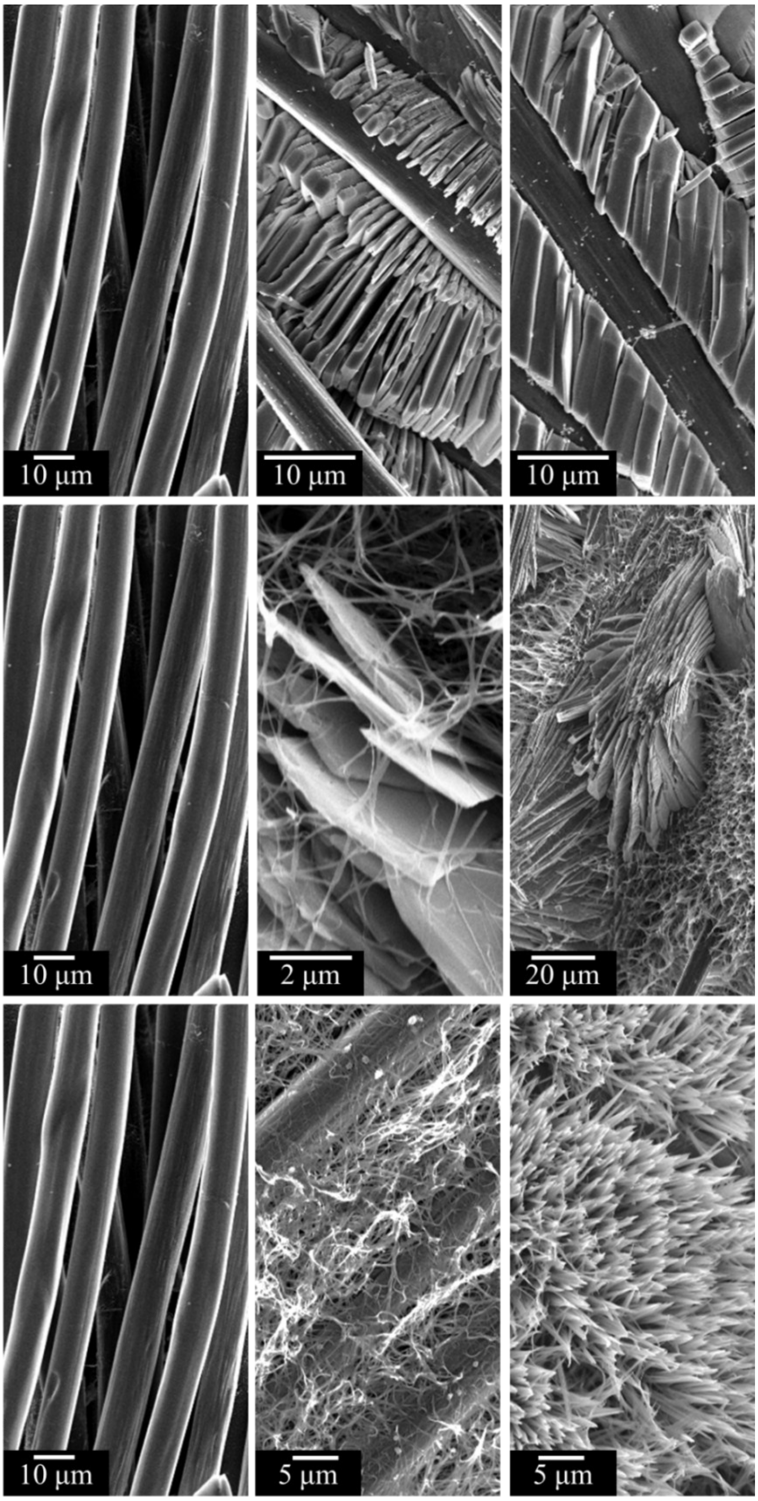

Fig. S2 Morphological evolution of $V_2O_5{\cdot}H_2O$ plotted as a function of the elapsed duration of deposition (horizontal row) and the ratio of Na_2SO_4 to NH_4VO_3 ratio (vertical column).

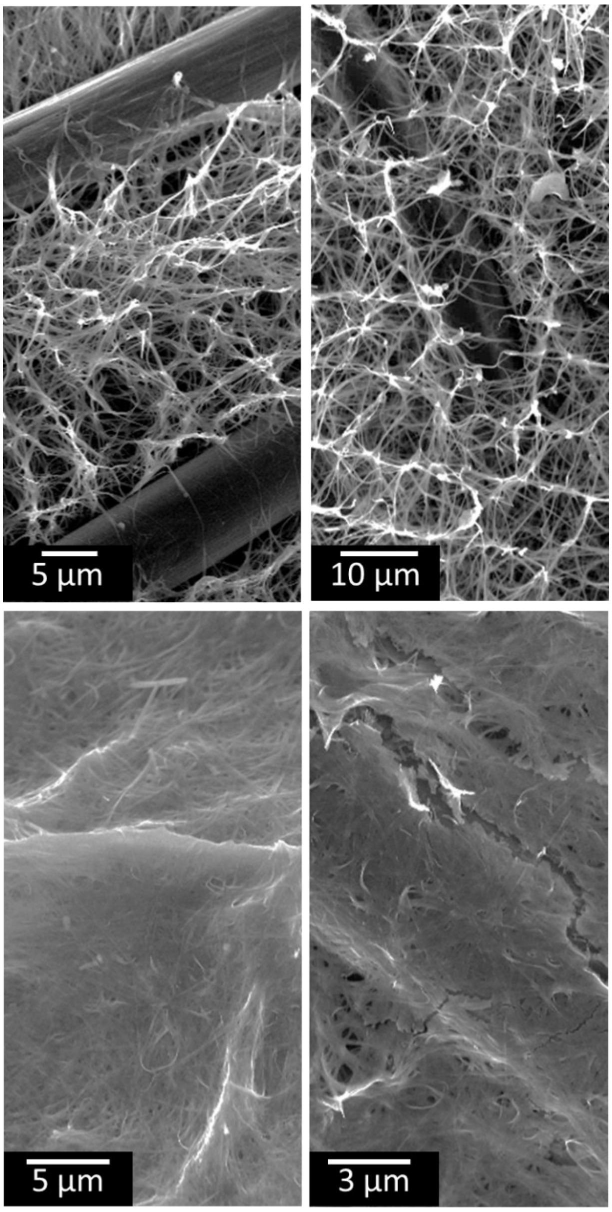

Fig. S3 Microtextural collapse of $V_2O_5{\cdot}H_2O$ as electroplating current density reached 2 mA cm^{-2}, characterized as a transformation from a porous network (upper row) to a dense film with visible cracks (lower row).

Performance evaluation of symmetric $V_2O_5{\cdot}H_2O/CC//V_2O_5{\cdot}H_2O/CC$ module in an operating potential range of 0-3.9 V. The electrochemical properties of symmetric $V_2O_5{\cdot}H_2O/CC//V_2O_5{\cdot}H_2O/CC$ supercapacitor were additionally characterized at an operating potential window (OPW) from 0 to 3.9V and the corresponding module performance were summarized in the Ragone plot (Fig. S4). Significantly, the $V_2O_5{\cdot}H_2O/CC$ module yet remarkably outperformed most state-of-the-art supercapacitors (Fig. S4c) in the footprint-normalized energy delivery with the highest value 1.99 mWh cm^{-2} (at small rate 1 mA cm^{-2}) and microbatteries (Fig. S4d) in the footprint-normalized power density up to 29.48 mW cm^{-2} (at high rate 10 mA cm^{-2}). These estimations were highly approximate to those made from the working diagrams acquired for the module studied in an identical configuration except the polarity of $V_2O_5{\cdot}H_2O/CC$ electrodes alternatively switched (Fig. 4 in the main text). The small disparities, namely a slightly minor energy density and othewrwise greater power delivery, arose presumably from the various extent in the Faradaic transitions of vanadia over different OPWs.[7] $V_2O_5 \cdot H_2O$/CC electrode probed in a symmetric configuration with a "damp" [EMIM][TFSI] as electrolyte is expected to undergo a one-electron-uptake/-release process at the potentail range of 0 – 3.9 V in two consecutive stages.

$$V_2O_5 \cdot H_2O + 0.5H_3O^+ + 0.5e^- \leftrightarrow H_{0.5}V_2O_5 \cdot 1.5H_2O \tag{7}$$

$$H_{0.5}V_2O_5 \cdot 1.5H_2O + 0.5H_3O^+ + 0.5e^- \leftrightarrow HV_2O_5 \cdot 2H_2O \tag{8}$$

Particularly, two characteristic phase transformations and the evidential color change (reddish yellow and gray green) are included in such course (inset in Fig. S4a), as well resolved in the sweep voltammogramm for the module cycled from -3.9 to 3.9 V at a scan rate 2 mV s^{-1} (Fig. 4a in the main text). Noteworthily, the sencond half-protonation step took place at the cell voltage approaching zero, where the inspected symmetric module nearly fully discharged. This featured phase-transition-potential suggested the discrepancy in energy density stemmed highly likely from a confined phase evolution for the module studied in a potential range of 0 – 3.9 V in terms of additional energy necessary to overcome the phase retention (hardly discernable in the CV scan (Fig. S4a) collected for the module tested under such condition).[8] Likewise, the concurrent enhancement in power delivery can be interpreted as the circumvention of sluggish kinetics specific to the phase transformation.

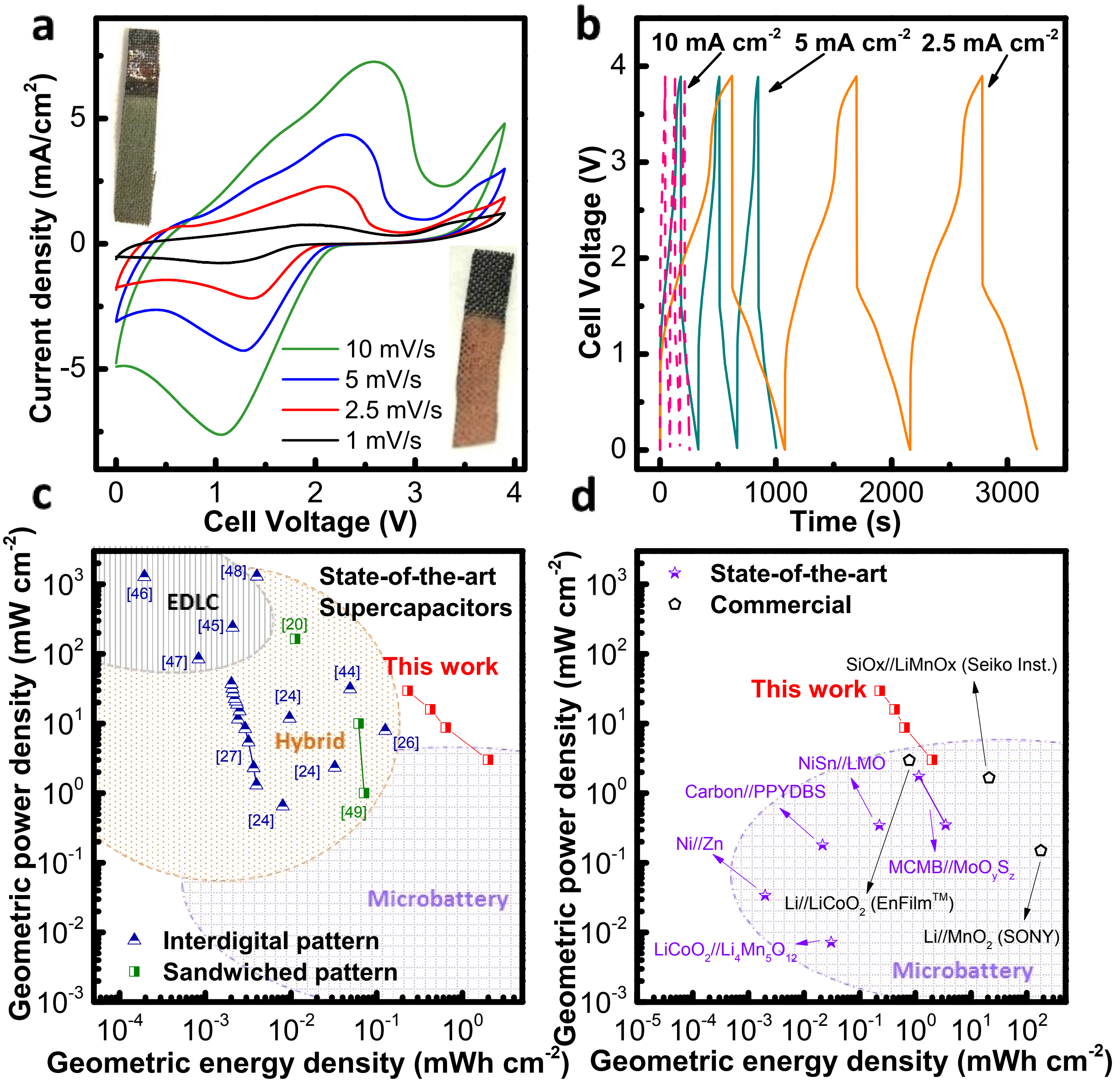

Fig. S4 (a) Cyclic voltammogramms and (b) galvanostatic charge and discharge curves of V_2O_5·H_2O/CC SSC in [EMIM][TFSI] at an operating potential window from 0 to 3.9 V with varied scan rate and current density, respectively. (c-d) Ragone plots of V_2O_5·H2O/CC SSC, commercial and EC at the state of the art, (c) and microbatteries (d) are plotted alongside for comparison. Inset: lithiated manganese oxide (LMO); dodecylbenzenesulfonatedoped polypyrrole (PPYDBS); mesocarbon microbeads (MCMB).

Structural evolution of V_2O_5·H_2O/CC electrode after cycling test in a symmetric module with [EMIM][TFSI] as the electrolyte. SEM and TEM studies on the V_2O_5·H_2O/CC electrode underwent a long-term stability examination in [EMIM][TFSI] electrolyte were additionally carried out to elucidate the outstanding cyclic performance from a structural viewpoint (Fig. S5). A geometric transition of V_2O_5·H_2O from a belt-like figure (Fig. S5a) to a sheet-analogous form (Fig. S5b) after 10,000 cycles was first perceived. Such transformation was interpreted as a result of the coalescence between closely neighbored V_2O_5·H_2O nanobelts in the literature due to a consecutive volume shrinkage and expansion upon the ion de-/intercalation during the cycling test.[9] Particularly, in this study the migration of the crystallization water from V_2O_5·H_2O into [EMIM][TFSI] electrolyte and *vice versa* was mostly responsible for this process in terms of the bulky volume of $[EMIM]^+$ and $[TFSI]^-$ restricting their insertions only at the oxide-RTIL boundary.

$$V_2O_5 \cdot H_2O + x[EMIM]^+ + xe^- \leftrightarrow [EMIM]_xV_2O_5 \cdot H_2O \ (interface - confined) \tag{9}$$

$$[EMIM]_xV_2O_5 \cdot H_2O + nH_3O^+ + ne^- \rightarrow [EMIM]_xH_nV_2O_5 \cdot (1+n)H_2O \tag{10}$$

Significantly, the minor pulverization of $V_2O_5 \cdot H_2O$ (Fig. S5b and insets in Fig. S5c,d) and the respectable retentions in the crystallographic and structural integrity (Fig. S5c,d) as well as in the porosity of the built-up network (Fig. S5b) evidently indicated the diffusion course of these proton-containing water media was highly reversible. More importantly, these evidences further corroborate the circumvention of undesirable injury to the electrode framework, leading to the exceptional electrochemical stability of the present system (Fig. 3b in the main text).

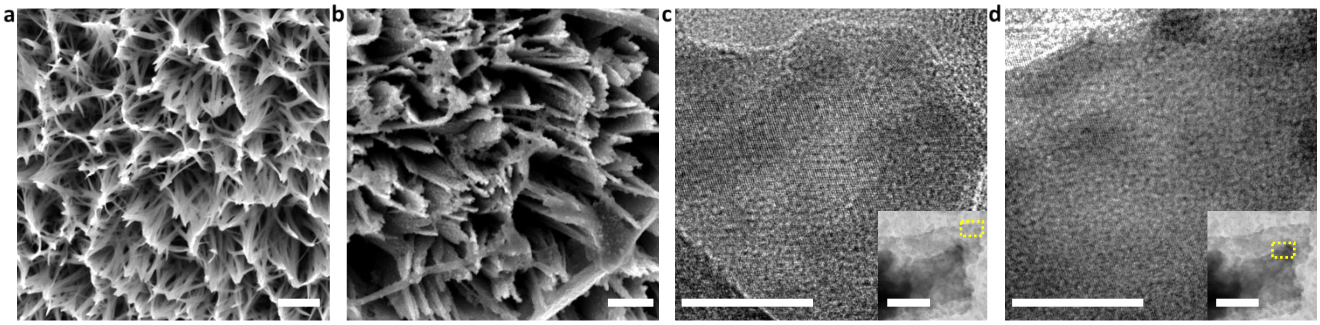

Fig. S5 SEM images collected for $V_2O_5 \cdot H_2O$/CC electrodes (a) before (scale bar: 3 µm) and (b) after (scale bar: 1 µm) the cyclic performance in [EMIM][TFSI] electrolyte. (c,d) HRTEM lattice images (scale bar: 20 nm) collected at the framed regions shown in the respective insets (scale bar: 100 nm) for $V_2O_5 \cdot H_2O$/CC electrode after the long-term stability investigation.

References

1 K. Kodama, R. Tsuda, K. Niitsuma, T. Tamura, T. Ueki, H. Kokubo and M. Watanabe, *Polym. J.,* 2011, **43**, 242.

2 L. Li, J. B. Zhang, Z. W. Peng, Y. L. Li, C. T. Gao, Y. S. Ji, R. Q. Ye, N. D. Kim, Q. F. Zhong, Y. Yang, H. L. Fei, G. D. Ruan and J. M. Tour, *Adv. Mater.*, 2016, **28**, 838.

3 J. Lin, Z. W. Peng, Y. Y. Liu, F. Ruiz-Zepeda, R. Q. Ye, E. L. G. Samuel, M. J. Yacaman, B. I. Yakobson and J. M. Tour, *Nat. Commun.*, 2014**, 5**, 5741.

4 M. B. Sassin, A. N. Mansour, K. A. Pettigrew, D. R. Rolison and J. W. Long, *ACS Nano*, 2010, **8**, 4505.

5 A. E. Fischer, K. A. Pettigrew, D. R. Rolison, R. M. Stroud and J. W. Long, *Nano Lett.*, 2007**, 7**, 281.

6 M. Beidaghi and Y. Gogotsi, *Energy Environ. Sci.*, 2014, **7**, 867.

7 D. Wei, M. R. J. Scherer, C. Bower, P. Andrew, T. Ryhanen and U. Steiner, *Nano Lett.*, 2012, **12**, 1857.

8 Y. K. Hsu, Y. C. Chen, Y. G Lin, L. C. Chen and K. H. Chen, *Chem. Commun.*, 2011, **47**, 1252.

9 G. M. Wang, X. H. Lu, Y. C. Ling, T. Zhai, H. Y. Wang, Y. X. Tong and Y. Li, *ACS Nano*, 2012, **6**, 10296.